Interplay of shape, interface structure, and electrostatic fields of ionic nanodots embedded in a polar semiconductor matrix

R. Leitsmann* and F. Bechstedt

European Theoretical Spectroscopy Facility (ETSF) and Institut für Festkörpertheorie und -optik, Friedrich-Schiller-Universität Jena, Max-Wien-Platz 1, 07743 Jena, Germany

(Received 8 August 2008; published 21 November 2008)

The structural, electrostatic, and electronic properties of PbTe nanocrystals (NCs) embedded in a CdTe matrix are investigated using an *ab initio* pseudopotential method and a repeated supercell approximation. The calculated dot-matrix interface geometries are in excellent agreement with the plane PbTe/CdTe interfaces. The constructed rhombo-cubo-octahedron shape of the NCs corresponds to the equilibrium crystal shape and transmission-microscopy observations. We demonstrate that polar interfaces with either cation or anion termination appear predominantly in one-half space with [111] or $[\bar{1}\bar{1}\bar{1}]$ orientation. This leads to the occurrence of a macroscopic electrostatic field, which superimposes that of the atoms. As a consequence an internal quantum-confined Stark effect is predicted. Its influence on the electronic states is discussed.

DOI: 10.1103/PhysRevB.78.205324 PACS number(s): 68.65.Hb, 68.35.Ct, 73.22.−f, 73.21.La

I. INTRODUCTION

Arrays of embedded quantum dots (QDs), which show quantum confinement effects for electrons and holes, are promising systems for applications in light-emitting diodes and lasers. They are grown within a Stranski-Krastanov growth mode or other self-organization processes. The dots are influenced directly and indirectly by their interfaces (with certain orientations), chemical bonds, polarities, ionicity differences, structural variations in the adjacent crystals, strain, and spontaneous or piezoelectric fields. The most famous example is the InAs/GaAs system with the same zinc-blende (zb) crystal structure and vanishing differences in the bulk bond ionicities but a large lattice-constant mismatch of about 7%. The nanoscale coherent InAs islands are often arranged in a regular array with a narrow size distribution.[1] Despite the [001] orientation of the GaAs substrate, the top InAs pyramidal facets are discussed in terms of nonpolar {110} cleavage faces[2,3] although scanning tunneling microscopy (STM) of free-standing InAs dots indicates higher index surfaces such as {137}.[4] However, there are also several other interesting material combinations of nanodots with well-defined interface facets and matrices such as Si nanocrystals in SiO_2,[5] CoO inclusions in ZnO,[6] or PbTe quantum dots (QDs) in a CdTe host.[7]

Application of an electric field on a quantum-well (QW) structure based on layers of two semiconductors leads to the quantum-confined Stark effect (QCSE).[8] On the other hand the QCSE can also be induced by an internal electric field, which is generated by polar interfaces, uniaxial or biaxial strain, or a spontaneous electric polarization. Layered structures, such as superlattices or multi-quantum-well arrangements, with the pairwise occurrence of A and B interfaces lead to an additional macroscopic electrostatic sawtooth potential due to the opposite interface charges.[9] The macroscopic mirror symmetry is broken. Consequently, the locally build electric field tends to spatially separate the maxima of the probability to find electrons and holes.[10] In layered heterostructures of common III-V compounds with zb structure grown in [001] direction, such as GaAs/AlAs(001), the strength of the internal electric fields almost vanishes due to the small mismatch in bond polarities and lattice constants. In contrast, heterostructures of wurtzite semiconductors with large bond ionicities and/or bond-length differences, such as GaN and InN alloys grown in [0001] direction, exhibit remarkable spontaneous and piezoelectric polarization fields,[11] which give rise to significant spectroscopic features, e.g., a redshift and a drastic intensity reduction in light emission.[12]

The question arises if strong internal electric fields, especially such ones induced by the presence of polar interfaces, may occur in embedded QDs with nearly centrosymmetric shape. Prototypical systems in which the answer to this question can be studied are PbTe QDs embedded in a CdTe matrix. High-resolution cross-sectional transmission electron microscopy (HRXTEM) studies[7,13] for annealed PbTe/CdTe systems have shown the existence of rather ideal PbTe nanocrystals with {111}, {100}, and {110} interfaces within the CdTe host material. There is seemingly an almost lack of asymmetries compared with other QDs prepared by Stranski-Krastanov growth, such as an interconnecting two-dimensional wetting layer, inhomogeneous alloying with the host material, or shape asymmetries.[14] The preceding annealing procedure and the almost vanishing lattice-constant mismatch between PbTe and CdTe suggest a situation close to thermal equilibrium for the nanostructured system. Therefore, the shape of the resulting quantum dots has been predicted using a combination of parameter-free total energy (TE) calculations and a Wulff construction according to the minimal free interface excess energies.[15] However, due to the pairwise occurrence of polar A and B interfaces of (111) and (100) types only averaged interface energies are taken into account in the interface simulations.

On the other hand the theoretical investigation of the tellurides, PbTe and CdTe, in particular of their surfaces and interfaces, is a challenging task for several reasons. There is a remarkable ionic contribution to the chemical bonding in PbTe and CdTe. Nevertheless, CdTe has a nonvanishing electron distribution around the Cd-Te connecting line suggesting a directional covalent contribution to its bonds.[16] For PbTe the coordination of the atoms is increased from four to

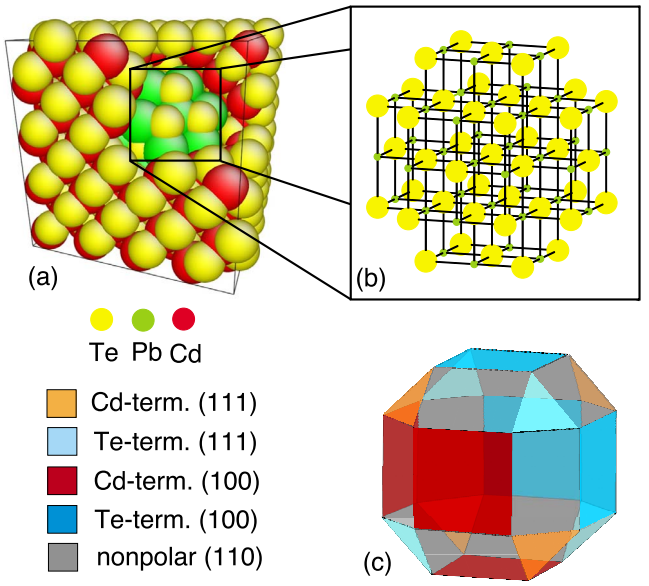

FIG. 1. (Color online) (a) Simple model of a PbTe NC embedded in a CdTe matrix. To enhance the visibility in the first quadrant no matrix atoms are shown. (b) Stick and ball model of a small embedded PbTe NC without matrix. (c) Schematic representation of the occurring dot-matrix interface facets. Different terminations are indicated by different colors.

six. As a consequence PbTe crystallizes in rocksalt (rs) structure with the space group $Fm3m$ (O_h^5), whereas the more covalent CdTe crystallizes in zb structure with space group $F\bar{4}3m$ (T_d^2). Despite the almost vanishing lattice-constant mismatch and the same fcc Bravis lattice, the material combination PbTe/CdTe exhibits a crystal-structure mismatch (rs-zb) and polar interfaces. The $\langle 100 \rangle$ orientations in zb structure lead to polar (cation or anion terminated) surfaces. In the $\langle 111 \rangle$ cases both crystal structures, rs and zb, give rise to polar interfaces. The resulting interface charges have consequences for the interface extent, the actual atomic positions, and moreover for the electrostatic fields.[13,15] However, even the isolated interfaces between strongly ionic materials are hardly understood. In general, abrupt polar interfaces are energetically less stable than interfaces with interdiffusion of atoms. Hence, they tend to build intermixed and reconstructed geometries.[17–19] These tendencies are however less pronounced for the tellurides combination.[15]

The QCSE due to an external electric field has already been discussed for quantum-dot structures (see, e.g., Ref. 20). However, the formation of internal electric fields in an embedded nanocrystal (NC) as a consequence of a certain arrangement of A and B interface facets with different crystallographic orientations (see Fig. 1) have not been studied so far. How the electrostatics or, more precisely, the actual electrostatic potential is influenced by the dot shape, the dot symmetry, and the distribution of polar interfaces is an open question. The combination of a rs-PbTe QD embedded in a zb-CdTe matrix can serve as a model system for corresponding studies.

In the present paper we investigate the structural and bonding properties of PbTe nanodots with various interface facets embedded in a CdTe matrix versus the QD size using *ab initio* methods. In particular, the accompanying internal local electric fields and their retroactive effects on the NC geometry are studied in Sec. II. The consequences for the atomic geometries, the energetic stability, and the occurrence of electrostatic potentials are discussed in Sec. III. Additionally, consequences of the eventually occurring electric field on the electronic states and related properties are indicated. Finally, in Sec. IV we will give a short summary and draw conclusions.

II. MODELING AND METHODS

A. Nanocrystal construction within supercells

The PbTe NCs embedded in a CdTe matrix are modeled using the so-called supercell method,[21] i.e., periodic boundary conditions are applied. A three-dimensional arrangement of nanocrystals embedded in a matrix material is considered. We use a simple-cubic arrangement of supercells. Each of them contains one QD (here, rs-PbTe) and a certain amount of the matrix material (here, zb-CdTe). The sizes of the simple-cubic supercells vary with the diameter of the NCs and the extent of the matrix between neighboring QDs.

Despite the almost vanishing lattice-constant mismatch between PbTe and CdTe and hence nearly the same lattice constants, the different coordinations of the atoms in rs- and zb-structure make the construction of the NC shape and the accompanying bonding configuration challenging. To generate reasonable start configurations for the ionic relaxation we use almost equilibrium crystal shapes (ECSs), which are used to divide the supercell into a matrix and a NC region. Both materials, PbTe and CdTe, crystallize in a fcc structure with a common Te sublattice. Therefore, we start the construction by setting up a Te fcc sublattice in the whole supercell. Thereby, in the center of the supercell can be either a Te atom or the center of a Te-Te connecting line (i.e., a Pb atom). In order to create the zb structure of CdTe and the rs structure of PbTe we continue locally with a second fcc lattice. It is displaced by a quarter of a body diagonal $(1,1,1)a_0/4$ in the matrix region and by half a body diagonal $(1,1,1)a_0/2$ in the NC region with respect to the Te sublattice. In this way we end up with a stoichiometric and electrostatic neutral supercell with the same number of cations and anions, while the PbTe NCs and the CdTe matrices are usually nonstoichiometric according to the counting during construction. Unfortunately this construction method leads to stacking faults at the (111) and $(\bar{1}\bar{1}\bar{1})$ dot-matrix interfaces, which have been corrected by transferring Cd atoms from a $(\bar{1}\bar{1}\bar{1})$ corner to a corresponding (111) corner of the NC.

According to the described procedure we have constructed supercell systems with different dot and matrix sizes, which are denoted as given in Table I. The denotation $nm(a/c)$ characterizes the number n of nearest-neighbor atom shells counted from the NC center, the edge length of the supercell ma_0 in units of the bulk lattice constant a_0, and the central atom, either a Te anion (a) or a Pb cation (c). In addition the NC-NC distance is given to describe the extent of the matrix between the surfaces of two neighbored NCs. According to the construction three different QD shapes oc-

TABLE I. Structural parameters of the constructed NC supercells.

Notation	Outermost NC shell	Atom in NC center	Supercell size in a_0	NC diameter in nm	NC-NC distance in nm	NC shape	Relative size of interface facets {100}:{110}:{111}
33*a*	3	Te	3	0.64	1.28	Cube	1:0:0
33*c*	3	Pb	3	0.64	1.28	Cube	1:0:0
43*a*	4	Te	3	1.28	0.64	Oct(1)	$1:\sqrt{2}:\frac{1}{3}$
43*c*	4	Pb	3	1.28	0.64	Oct(1)	$1:\sqrt{2}:\frac{1}{3}$
44*a*	4	Te	4	1.28	1.28	Oct(1)	$1:\sqrt{2}:\frac{1}{3}$
44*c*	4	Pb	4	1.28	1.28	Oct(1)	$1:\sqrt{2}:\frac{1}{3}$
45*a*	4	Te	5	1.28	1.92	Oct(1)	$1:\sqrt{2}:\frac{1}{3}$
45*c*	4	Pb	5	1.28	1.92	Oct(1)	$1:\sqrt{2}:\frac{1}{3}$
55*a*	5	Te	5	1.92	1.28	Oct(2)	$1:2\sqrt{2}:\frac{4}{3}$
55*c*	5	Pb	5	1.92	1.28	Oct(2)	$1:2\sqrt{2}:\frac{4}{3}$
55sph	5	Te	5	1.92	1.28	Sphere	

cur: cubes, rhombo-cubo-octahedrons, and spheres. They differ with respect to the relative contributions from the {100}, {110}, and {111} facets. In the case of the cubes only {100} facets occur. The rhombo-cubo-octahedrons are regular octahedrons with {111} facets truncated at each apex by {100} planes perpendicular to the cube axis. They are distorted by additional {110} facets between the other ones (see, e.g., Fig. 1). The areas of the six {100} facets, the 12 {110} facets, and the eight {111} facets occur in two different ratios, $1:\sqrt{2}:\frac{1}{3}$ [oct(1)] and $1:2\sqrt{2}:\frac{4}{3}$ [oct(2)]. In the case of the largest NCs under consideration we also study a more or less spherical shape denoted by "sph."

Independent of the shape and the facets all generated structures exhibit a C_{3v} symmetry with the symmetry axis along the [111] direction. This symmetry reduction in the original O_h (PbTe) and T_d (CdTe) point groups is related to the inequality of oppositely terminated but for reasons of electrostatic neutrality pairwise occurring dot-matrix interfaces as schematically shown in Fig. 1. Using the notation of Ref. 15 we find Cd-terminated dot-matrix interfaces at the $(\bar{1}00)$, $(0\bar{1}0)$, $(00\bar{1})$, (111), $(1\bar{1}\bar{1})$, $(\bar{1}\bar{1}1)$, and $(\bar{1}1\bar{1})$ faces and Te-terminated dot-matrix interfaces at the (100), (010), (001), $(\bar{1}\bar{1}\bar{1})$, $(\bar{1}11)$, $(11\bar{1})$, and $(1\bar{1}1)$ faces. Interestingly, those facet orientations lead to a dominance of the cation-terminated faces at the $[\bar{1}\bar{1}\bar{1}]$ halves of the NCs and vice versa of the anion-terminated faces at the [111] halves. Since Te(Cd)-terminated interfaces exhibit negative (positive) interface charges, one expects strong electrostatic fields along the [111] direction, which will have (as we will show below) a considerable influence on the structure and the electronic states.

B. Total-energy calculation

We apply the density-functional theory (DFT) within local-density approximation (LDA) as implemented in the Vienna *ab initio* simulation package (VASP).[22,23] Since the influence of nonscalar relativistic effects (in particular spin-orbit coupling) on the structural data is negligible[15] we do not take those effects into account. The interaction of the valence electrons with the remaining ions is modeled by pseudopotentials generated within the projector augmented wave (PAW) method.[24] In II-VI and IV-VI semiconductors the outermost occupied *d* states give rise to shallow semicore states, which contribute essentially to the chemical bonding.[25] Therefore, we treat the Cd 4*d* and Pb 5*d* electrons as valence electrons. An energy cutoff of 15 Ry for the plane-wave basis is sufficient to obtain converged structural properties. The total-energy expression contains a Brillouin-zone (BZ) integration, which is replaced by a summation over special points of the Monkhorst-Pack (MP) type.[26] However, the large size of the supercells justifies (at least for the structural relaxation) the restriction of the **k**-point sampling in the BZ to the Γ point. Since the two cubic crystals CdTe and PbTe have nearly the same lattice constants a_0, we use an average (theoretical) constant of $a_0=6.41$ Å. The small lattice-constant misfit of less than 0.4% is neglected, whereas the lattice-type mismatch is taken into account. Ionic relaxation of the starting geometries and element distributions are allowed. The atomic equilibrium positions are obtained for Hellmann-Feynman forces smaller than 20 meV/Å in each x, y, z component. The resulting geometries are used to derive bond length (or nearest-neighbor distances) and interface bonding configurations. For the equilibrium positions and the electron density that minimize the total energy, we solve the Kohn-Sham equation. The local part of its single-particle potential without the exchange-correlation part will be herein referred to as electrostatic potential. The energy eigenvalues are later used to discuss the electronic structure of the embedded NCs.

III. RESULTS AND DISCUSSION

A. Bond lengths

All optimized structures except NC 33*a* (Table I) keep the C_{3v} symmetry of their starting configurations. The small NC 33*a* should be better characterized as a large molecular structure so that the changes after relaxation are much larger. The ionic relaxation yields disturbed lattice structures. Special

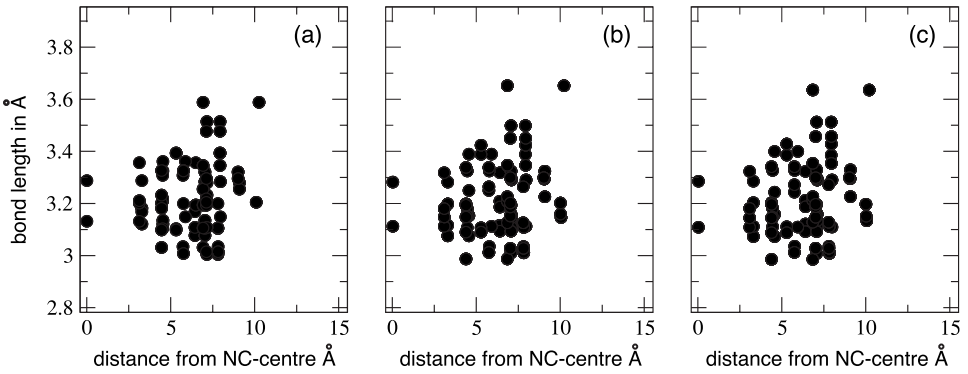

FIG. 2. Te-Pb bond length for (a) dot43, (b) dot44, and (c) dot45 QDs. The horizontal line indicates the corresponding distance in bulk rs-PbTe.

measures are the nearest-neighbor distances in the original rs-like PbTe NCs. They deviate from the bulk value $a_0/2 = 3.205$ Å as shown in Figs. 2 and 3. Figure 2 compares the Pb-Te bond lengths obtained for PbTe NCs with the same diameter of 1.28 nm but for different supercell sizes. As clearly seen the bond-length distribution of dot 43*a* differs slightly from the results obtained for 44*a* and 45*a*. This is caused by the relatively small NC-NC distances[27] implied by the periodic boundary conditions of the supercell method. As a consequence interactions across the matrix region are possible and influence the dot-matrix interface geometries. On the other hand, the comparison of the results for dots 44*a* and 45*a* indicates that NC-NC distances of at least 1.28 nm are sufficient to obtain converged results for the atomic displacements. In Fig. 3 the results of the geometry optimization for three different dot sizes and different central atoms are shown. Again, we have plotted the Te-Pb bond length versus the NC radius. The results of the structural optimization in Figs. 2 and 3 are in contrast to those obtained for hydrogenated Si and Ge NCs, which show the general tendency to increase the bond lengths (tensile strain) in the NC core region but to decrease the bond lengths in the outermost regions (compressive strain).[28] Thereby, these effects are most pronounced for dots with small radii. Here, we find no clear radial dependence of the bond-length distribution for the embedded PbTe NCs. Enlargement and shortening of the Te-Pb distances occur for all radial distances from the QD center. Nevertheless, two main structural effects can be identified.

First of all we observe a tendency to form bilayers along the symmetry axis [111] in PbTe dots. This results in two different bond lengths: an intrabilayer bond length and an interbilayer bond length. The averages of both kinds are indicated in Fig. 3 by solid and dashed lines. The deviations from the bulk PbTe bond length are about 9% for 33*c*, 6% for 33*a*, 44*a*, 44*c*, and 55*a*, and 3% for 55*c*. Consequently, one cannot state a clear size dependence. However, since this effect is the result of the electrostatic field along the [111] direction (as demonstrated below) we expect it to vanish for very large dot sizes. This trend is indeed visible in Fig. 3 for the NCs with a Pb atom in the center. For the QDs with a Te atom in the center the studied sizes remain too small to approach the bulk length.

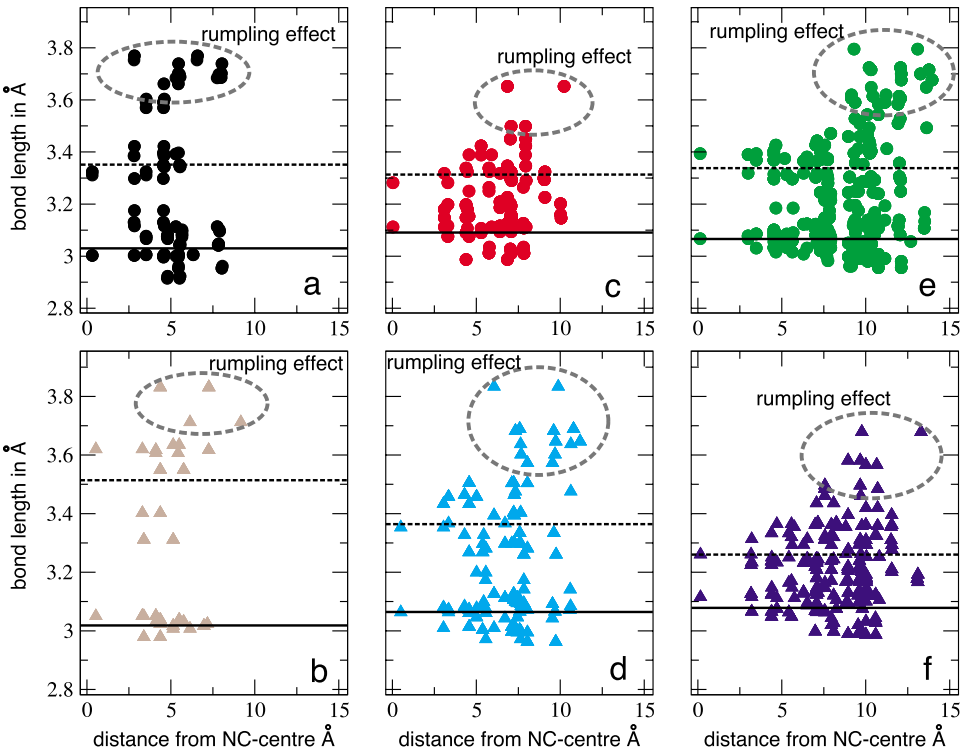

FIG. 3. (Color online) Pb-Te bond length for (a) 33*a*, (b) 33*c*, (c) 44*a*, (d) 44*c*, (e) 55*a*, and (f) 55*c*. The dashed horizontal lines represent the average interbilayer bond length, while the solid horizontal lines represent the average intrabilayer bond length. The increased bond lengths (indicated by a dashed ellipse) at the $(\bar{1}00)$, $(0\bar{1}0)$, and $(00\bar{1})$ dot matrix interfaces are related to a rumpling effect.

The second effect visible in Figs. 2 and 3 is the so-called rumpling effect.[29] As shown in Ref. 15 for flat Cd-terminated PbTe/CdTe(100) interfaces one observes an inward shift of the Pb atoms of the order of 0.4 Å, resulting in an enlarged Pb-Te interface bond length. This is in excellent agreement with the 0.4–0.5 Å larger Pb-Te bond length observed at the $(\bar{1}00)$, $(0\bar{1}0)$, and $(00\bar{1})$ dot-matrix interface facets. In Fig. 3 we have indicated those values by dashed ellipses. In contrast, the (100), (010), and (001) dot-matrix interface facets exhibit a much smaller rumpling effect, which is again in excellent agreement with the results for flat Te-terminated PbTe/CdTe(100) interfaces.[15] Due to the combination of facets to an entire dot-matrix interface, i.e., for symmetry reasons, the lateral offset parallel to PbTe/CdTe(110) interfaces discussed in Ref. 15 cannot occur at interfaces of embedded PbTe NCs.

Summarizing the results presented in Figs. 2 and 3 one observes a trimodal behavior of the nearest-neighbor bond lengths in the rs-NCs, rather independent of their distances to the NC center. Two modes (intrabilayer and interbilayer distances) are consequences of the electrostatic forces acting on cation or anion {111} planes. The reason for the emergence of those electrostatic forces will be discussed in detail in Sec. III C. The third mode (rumpling effect) with the largest Te-Pb distances occurs around the Cd-terminated {100} interfaces. It is the result of an effect that already appears at planar interfaces. Experimentally, the main aspects of the theoretical predictions for the {100} interface geometries (at both planar and dot-matrix interfaces) are confirmed. In particular the pairwise occurring of differently terminated dot-matrix facets at opposite quantum dot sides have been observed by HRXTEM studies.[30] However, similar studies have reported a tendency for elongation of embedded PbTe QDs in one direction.[31] This direction has been interpreted to be the [001] in agreement with the layer orientation of the originally grown PbTe layer.

B. NC stability

To analyze the stability of the investigated embedded PbTe NCs we calculate the so-called dot formation energy,

$$E_f = E_{\mathrm{tot}} - [(N_{\mathrm{Te}}^d + N_{\mathrm{Te}}^m)\mu_{\mathrm{Te}} + N_{\mathrm{Pb}}\mu_{\mathrm{Pb}} + N_{\mathrm{Cd}}\mu_{\mathrm{Cd}}], \quad (1)$$

assuming that the system is formed by atoms from reservoirs with the chemical potentials μ_{Te}, μ_{Pb}, and μ_{Cd}. The total number of Te atoms is the sum of the corresponding atoms in the dot and matrix region, $N_{\mathrm{Te}}=N_{\mathrm{Te}}^d+N_{\mathrm{Te}}^m$. Due to the applied stoichiometry and the electrostatic neutrality it holds $N_{\mathrm{Te}}=N_{\mathrm{Pb}}+N_{\mathrm{Cd}}$. The experimental preparation of the NCs starts from relatively thick [001] oriented CdTe and PbTe layers.[7] These material layers form reservoirs for the atoms contributing to the dot-matrix system during a rapid thermal annealing (RTA) process. We assume that the resulting PbTe NCs and the matrix material are nearly in a thermal equilibrium, i.e.,

$$\mu_{\mathrm{CdTe}}^{\mathrm{bulk}} = \mu_{\mathrm{Cd}} + \mu_{\mathrm{Te}} \quad \text{and} \quad \mu_{\mathrm{PbTe}}^{\mathrm{bulk}} = \mu_{\mathrm{Pb}} + \mu_{\mathrm{Te}}. \quad (2)$$

With definition (1) these conditions lead to

TABLE II. NC interface energy γ [Eq. (4)] for different NC shapes. To minimize errors resulting from different k-point densities we have normalized all values to $\gamma^{(\mathrm{oct1})}$ of the corresponding supercell size.

Central atom	Cube	Oct(1)	Oct(2)	Sphere
Te	1.91	1.00	1.26	1.30
Pb	2.07	1.36	0.86	

$$E_f = E_{\mathrm{tot}} - N_{\mathrm{Pb}}\mu_{\mathrm{PbTe}}^{\mathrm{bulk}} - N_{\mathrm{Cd}}\mu_{\mathrm{CdTe}}^{\mathrm{bulk}}. \quad (3)$$

The formation energy [Eq. (3)] can also be related to an interface energy between the dot and the matrix. Since it depends on the actual size of the NC (Ref. 32) or more precisely on the size of the dot-matrix interface A_{O}, we introduce a normalized energy,

$$\gamma = \frac{E_f}{A_{\mathrm{O}}}, \quad (4)$$

which is essentially the NC interface energy per unit area. In Table II the interface energies for different NC shapes are listed. The abbreviations oct(1) and oct(2) denote rhombo-cubo-octrahedron NC shapes with different relative sizes of their interface facets (see Table I). The stability of a certain dot-matrix system depends very much on the interface shape and the central atom. Table II indicates that faceted interfaces with the simultaneous appearance of {100}, {110}, and {111} facets give rise to the most stable dot-matrix systems. The two extremum shapes, cube with {100} facets and sphere, are energetically less favorable. The ratio of the facet areas on the distorted rhombo-cubo-octrahedrons depends on the chemical nature of the central atom. In the case of an anion in the center the lowest energy appears for a ratio of the {100}, {110}, and {111} areas of $1:\sqrt{2}:\frac{1}{3}$, while for a cation in the center the ratio $1:2\sqrt{2}:\frac{4}{3}$ is preferred. The strong dependence of the NC stability on the central atom is the result of differences in the atomic displacements at the dot-matrix interfaces. As can be seen in Fig. 3. The distortion of the Te-Pb interface bond length is larger for 44c and 55a compared to 44a and 55c. Such an increase in the bond length will of course lead to an increased in interface energy γ and hence a decreased in NC stability.

C. Electrostatic fields

Due to the construction principle (i.e., one atom in the supercell center) the dot-matrix interfaces exhibit facets with different polarity at opposite NC sides. Therefore, one expects a residual electrostatic field created by the interface charges at the polar {111} and {100} interface facets [see Fig. 1(c)]. To visualize this effect we have calculated the electrostatic potential acting on a Kohn-Sham electron from the Hartree contribution and the local part of the electron-ion interaction. We are interested only in macroscopic or mesoscopic fields, i.e., in fields with characteristic lengths of spatial variations in the order of the NC size. Mainly the variations of the electrostatic potential due to the arrangement of

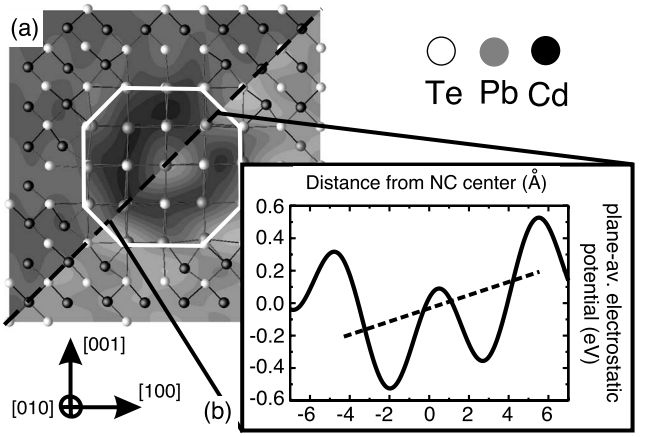

FIG. 4. (a) Fourier-filtered electrostatic potential (arbitrary units) shown in the $(\bar{1}10)$ and $(0\bar{1}1)$ planes. Dark gray corresponds to negative values and light gray to positive values. The atomic positions of PbTe NC (inside the white line) and matrix are indicated by a stick and ball model. (b) The solid line shows the plane average of the Fourier-filtered electrostatic potential along the [111] direction. The estimated slope of the electrostatic potential inside the dot region is indicated by a black dashed line.

Pb and Cd atoms in dot and matrix are of interest. Variations as a consequence of the electron distributions around individual atoms (e.g., the d electrons of the cations) and the electron redistribution by the bonding of adjacent atoms should not be discussed. For that reason we perform a spatial average over characteristic distances of the order of the bond lengths or even smaller. This can be done using a Fourier filter.

In Fig. 4 (upper part) results for the Fourier-filtered electrostatic potential using a cut-off wavelength of 6.41 Å are shown. The offset between the averaged electrostatic potential in the dot and matrix regions is clearly visible. It is of the same order (~3 eV) as observed at flat PbTe/CdTe interfaces.[15] It indicates the electronic confinement of Kohn-Sham electrons (not of the effective-mass-like electrons and holes) within the PbTe QD. The same projections onto two equivalent planes $(\bar{1}10)$ and $(0\bar{1}0)$ indicate the C_{3v} symmetry of the dot-matrix system. The asymmetry of the potential along the [111] axis is also clearly visible. It is a consequence of the asymmetric distribution of Cd- and Te-terminated interface facets shown in Fig. 1(c). Similarly to what one knows from layered structures, e.g., superlattices, where the atomic oscillations of the electrostatic potential are superimposed by a mesoscopic or macroscopic saw-tooth potential in one dimension, the dot-matrix system exhibits a similar effect in three dimensions. However, along the [111] direction the features known from a superlattice appear as well. This has been demonstrated in the lower part of Fig. 4 where we show the plane average of the Fourier-filtered electrostatic potential along the [111]-symmetry axis of the system. Superimposed to the long-periodic dot-matrix oscillations one finds a triangular potential. In reality this additional mesoscopic/macroscopic potential represents a rounded saw-tooth potential in [111] direction with a characteristic increase or decrease in the dot or matrix region, respectively. It

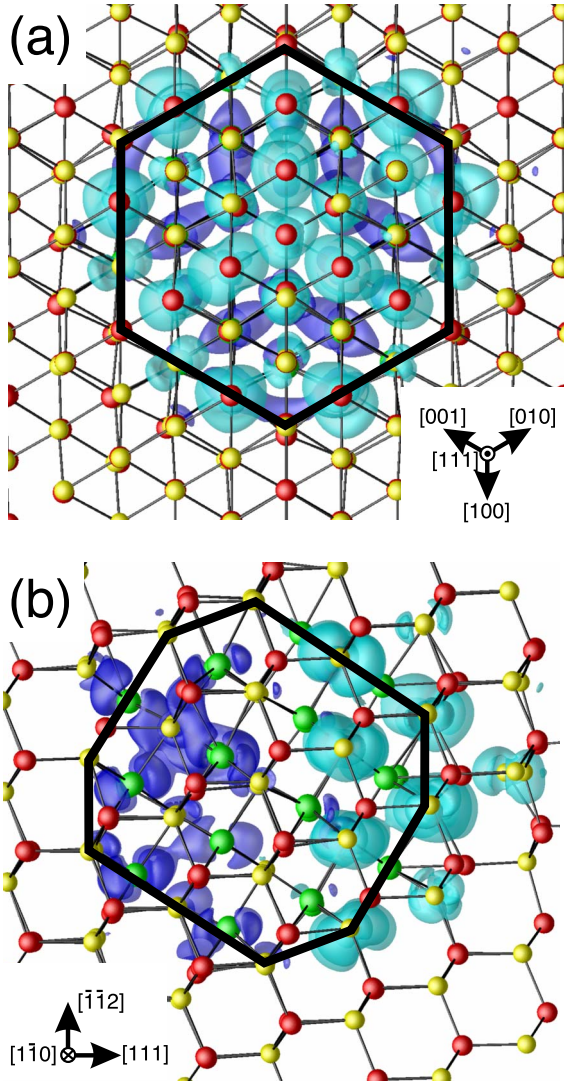

FIG. 5. (Color online) Isosurfaces of the HONO (cyan; light gray) and LUNO (blue; dark gray) states in an embedded PbTe QD (indicated by the solid black line). Te, Cd, and Pb atoms are shown in yellow (light gray), red, and green (dark gray), respectively. (a) Distribution perpendicular to the symmetry axis [111] and (b) distribution along the [111] axis.

is the result of the interface charge distribution. Its consequences on the structural properties have already been discussed in Sec. II A.

The macroscopic part (i.e., without the atomic oscillations) of the electrostatic potential plotted in Fig. 4 may be modeled starting from a reasonable description of the distribution of positive and negative dot-matrix interface charges. Assuming a spherical QD with radius r_0 the interface charges per unit area may be modeled by

$$\sigma(\vartheta) = \sigma_0 \cos \vartheta, \tag{5}$$

where we have used polar coordinates (r, ϑ, φ) (despite cylindric symmetry) with the z coordinate parallel to the [111] axis. The different dot and matrix materials are modeled using macroscopic dielectric constants ε_D and ε_M. The corresponding electrostatic problem can be solved analyti-

cally and the electrostatic potential follows as:

$$V(r,\vartheta) = \frac{\sigma(\vartheta)}{\varepsilon_0(2\varepsilon_M + \varepsilon_D)}\left[\Theta(r-r_0)\frac{r_0^3}{r^2} + \Theta(r_0-r)r\right]. \quad (6)$$

It yields an electrostatic field,

$$\mathbf{E}(r,\vartheta) = \frac{\sigma_0}{\varepsilon_0(2\varepsilon_M + \varepsilon_D)}\left[\Theta(r-r_0)\frac{r_0^3}{r^3}(2\mathbf{e}_r \cos\vartheta + \mathbf{e}_\vartheta \sin\vartheta) + \Theta(r_0-r)(-\mathbf{e}_r \cos\vartheta + \mathbf{e}_\vartheta \sin\vartheta)\right]. \quad (7)$$

With $\mathbf{e}_z = \mathbf{e}_r \cos\vartheta - \mathbf{e}_\vartheta \sin\vartheta$ the appearance of a constant electric field,

$$\frac{-\sigma_0}{\varepsilon_0(2\varepsilon_M + \varepsilon_D)}, \quad (8)$$

in z direction within the dot region is obvious. Using our *ab initio* results for NC 44*a* it can be estimated to a value of about 4.4 MV/cm. With $\varepsilon_{\mathrm{PbTe}}=35$ (Ref. 33) and $\varepsilon_{\mathrm{CdTe}}=10$ (Ref. 34) we obtain $\sigma_0=0.014$ electrons per Å^2 for NC 44*a*. However, since the interface charge σ results from polar interface facets (and not of free charges) it is proportional to $\frac{1}{r_0}$. Therefore, one obtains for experimentally observed QD sizes (e.g., 20 nm) values of about 6×10^{-4} electrons per Å^2.

As a consequence of the asymmetric distribution of the positive and negative interface charges along [111] we expect electronic properties significantly affected by the electrostatic field in the system, e.g., the distribution of the highest occupied NC orbital (HONO) as well as of the lowest unoccupied NC orbital (LUNO) is remarkably influenced. For NC 44*a* an isosurface of these two orbitals is plotted in Fig. 5. The corresponding maxima of the probability to find a hole or an electron are spatially separated. This so-called quantum-confined Stark effect is a consequence of the internal electric field, which gives rise to opposite displacements parallel to [111] of the electrons and holes, respectively. One possible consequence of the predicted QCSE could be an intensity reduction in the photoluminescence signal at very low temperatures due to the reduced oscillator strengths of the lowest optical transitions. Recently such an effect was indeed observed by Schwarzl *et al.*[35]

IV. SUMMARY AND CONCLUSIONS

We have investigated nanocrystals consisting of heavily ionic materials (PbTe) embedded in a matrix of a polar semiconductor (CdTe) by means of *ab initio* methods. Quantum dots and matrix possess different crystal structures, rs and zb, but almost the same cubic lattice constants. Three types of quantum dot shapes—cube, rhombo-cubo-octrahedron with varying ratios of facet areas, and sphere—have been studied. Independent of the chemical nature of the central dot atom and despite the pairwise occurrence of cation-terminated and anion-terminated interface facets, the dot construction yields a dominance of the cation-terminated interfaces in the half space around the $[\bar{1}\bar{1}\bar{1}]$ corner, while the anion-terminated faces occur in the other half space. This leads to a symmetry break along the [111] direction resulting in an internal electric field induced by the interface charges. Despite of the nearly centrosymmetric shape of the NCs, the atomic core positions and the electronic states are influenced by this symmetry break. The induced electrostatic fields yield a tendency to form bilayers along the [111] symmetry axis. The obtained results for the dot-matrix interface geometries are in excellent agreement with previous results for flat PbTe/CdTe interfaces and experimental observations.

The accompanying electrostatic potential within the dot-matrix system is strongly influenced by the interface charges and exhibits a C_{3v} symmetry. In direction parallel to [111] it is superimposed by a potential variation over the characteristic extents of the dot and matrix with similarities to the saw-tooth potential appearing in superlattices. As a consequence of the modification of the arising potential within the dot we predict the occurrence of a quantum-confined Stark effect. Hence, the maxima of the electron and hole distributions are spatially separated along the [111] axis.

ACKNOWLEDGMENTS

We acknowledge valuable discussions with F. Schäffler, W. Heiss, F. Ortmann, J. Furthmüller, and F. Fuchs. The work was financially supported through the Fonds zur Förderung der Wissenschaftlichen Forschung (Austria) under Grant No. SFB25, Nanostrukturen für Infrarot-Photonik (IR-ON), and the EU NANOQUANTA network of excellence (Grant No. NMP4-CT-2004-500198). Grants of computer time from the Höchstleistungsrechenzentrum Stuttgart are gratefully acknowledged.

*roman@ifto.physik.uni-jena.de

[1] R. Heitz, T. R. Ramachandran, A. Kalburge, Q. Xie, I. Mukhametzhanov, P. Chen, and A. Madhukar, Phys. Rev. Lett. **78**, 4071 (1997).
[2] V. A. Shchukin and D. Bimberg, Rev. Mod. Phys. **71**, 1125 (1999).
[3] L. G. Wang, P. Kratzer, N. Moll, and M. Scheffler, Phys. Rev. B **62**, 1897 (2000).
[4] K. Jacobi, L. Geelhaar, and J. M. Marquez, Appl. Phys. A: Mater. Sci. Process. **75**, 113 (2002).
[5] G. Hadjisavvas, I. N. Remediakis, and P. C. Kelires, Phys. Rev. B **74**, 165419 (2006).
[6] K. Ueda, H. Tabata, and T. Kawai, Appl. Phys. Lett. **79**, 988 (2001).
[7] W. Heiss, H. Groiss, E. Kaufmann, M. Böberl, G. Springholz, F. Schäffler, K. Koike, H. Harada, and M. Yano, Appl. Phys. Lett. **88**, 192109 (2006).
[8] D. A. B. Miller, D. S. Chemla, and S. Schmitt-Rink, Phys. Rev. B **33**, 6976 (1986).
[9] R. Leitsmann and F. Bechstedt, Phys. Rev. B **76**, 125315 (2007).

[10] P. Harrison, *Quantum Wells, Wires and Dots* (Wiley, New York, 2005).
[11] E. T. Yu, X. Z. Dang, P. M. Asbeck, S. S. Lan, and G. J. Sullivan, J. Vac. Sci. Technol. B **17**, 1742 (1999).
[12] T. Takeuchi, C. Wetzel, G. Yamaguchi, H. Sakai, H. Amano, and I. Akasaki, Appl. Phys. Lett. **73**, 1691 (1998).
[13] R. Leitsmann, L. E. Ramos, F. Bechstedt, H. Groiss, F. Schäffler, W. Heiss, K. Koike, H. Harada, and M. Yano, New J. Phys. **8**, 317 (2006).
[14] J. Stangl, V. Holy, G. Bauer, and C. B. Murray, Rev. Mod. Phys. **76**, 725 (2004).
[15] R. Leitsmann, L. E. Ramos, and F. Bechstedt, Phys. Rev. B **74**, 085309 (2006).
[16] J. P. Walter and M. L. Cohen, Phys. Rev. B **4**, 1877 (1971).
[17] W. A. Harrison, E. A. Kraut, J. R. Waldrop, and R. W. Grant, Phys. Rev. B **18**, 4402 (1978).
[18] R. M. Martin, J. Vac. Sci. Technol. **17**, 978 (1980).
[19] M. Städele, J. A. Majewski, and P. Vogl, Phys. Rev. B **56**, 6911 (1997).
[20] S. A. Empedocles and M. G. Bawendi, Science **278**, 2114 (1997).
[21] M. C. Payne, M. P. Teter, D. C. Allan, T. A. Arias, and J. D. Joannopoulos, Rev. Mod. Phys. **64**, 1045 (1992).
[22] G. Kresse and J. Furthmüller, Comput. Mater. Sci. **6**, 15 (1996).
[23] G. Kresse and J. Furthmüller, Phys. Rev. B **54**, 11169 (1996).
[24] G. Kresse and D. Joubert, Phys. Rev. B **59**, 1758 (1999).
[25] S.-H. Wei and A. Zunger, Phys. Rev. B **37**, 8958 (1988).
[26] H. J. Monkhorst and J. D. Pack, Phys. Rev. B **13**, 5188 (1976).
[27] The notation NC-NC distance refers to the distance between the surfaces of neighboring quantum dots.
[28] H. C. Weissker, J. Furthmüller, and F. Bechstedt, Phys. Rev. B **67**, 245304 (2003).
[29] A. A. Lazarides, C. B. Duke, A. Paton, and A. Kahn, Phys. Rev. B **52**, 14895 (1995).
[30] H. Groiss, Diplomarbeit, Johannes Kepler University Linz, 2006.
[31] H. Groiss, E. Kaufmann, G. Springholz, T. Schwarzl, G. Hesser, F. Schäffler, W. Heiss, K. Koike, T. Itakura, T. Hotei, M. Yano, and T. Wojtowicz, Appl. Phys. Lett. **91**, 222106 (2007).
[32] In the limits N_{Cd} or $N_{Pb} \rightarrow 0$ it vanishes.
[33] E. A. Albanesi, E. L. P. y Blanca, and A. G. Petukhov, Comput. Mater. Sci. **32**, 85 (2005).
[34] I. Strzalkowski, S. Joshi, and C. R. Crowell, Appl. Phys. Lett. **28**, 350 (1976).
[35] T. Schwarzl, E. Kaufmann, G. Springholz, K. Koike, T. Hotei, M. Yano, and W. Heiss, Phys. Rev. B **78**, 165320 (2008).